nature catalysis

SUPPLEMENTARY INFORMATION

https://doi.org/10.1038/s41929-018-0085-6

In the format provided by the authors and unedited.

The stability number as a metric for electrocatalyst stability benchmarking

Simon Geiger[1,7]*, Olga Kasian[1,7], Marc Ledendecker[1], Enrico Pizzutilo[1], Andrea M. Mingers[1], Wen Tian Fu[2], Oscar Diaz-Morales[2], Zhizhong Li[3], Tobias Oellers[4], Luc Fruchter[3], Alfred Ludwig[4], Karl J. J. Mayrhofer[1,5,6], Marc T. M. Koper[2] and Serhiy Cherevko[1,5]*

[1]Department of Interface Chemistry and Surface Engineering, Max-Planck-Institut für Eisenforschung GmbH, Düsseldorf, Germany. [2]Leiden Institute of Chemistry, Leiden University, Leiden, the Netherlands. [3]Laboratoire de Physique des Solides, CNRS, Université Paris-Sud, Orsay, France. [4]Institute for Materials, Ruhr-Universität Bochum, Bochum, Germany. [5]Helmholtz-Institute Erlangen-Nürnberg for Renewable Energy (IEK-11), Forschungszentrum Jülich GmbH, Erlangen, Germany. [6]Department of Chemical and Biological Engineering, Friedrich-Alexander-Universität Erlangen-Nürnberg, Erlangen, Germany. [7]These authors contributed equally: Simon Geiger, Olga Kasian. *e-mail: geiger@mpie.de; s.cherevko@fz-juelich.de

Supplementary information:

The stability number as a metric for electrocatalyst stability benchmarking

Simon Geiger[a,†,*], Olga Kasian[a,†], Marc Ledendecker[a], Enrico Pizzutilo[a], Andrea M. Mingers[a], Wen Tian Fu[b], Oscar Diaz-Morales[b], Zhizhong Li[c], Tobias Oellers[d], Luc Fruchter[c], Alfred Ludwig[d], Karl J. J. Mayrhofer[a,e,f], Marc T. M. Koper[b], Serhiy Cherevko[a,e,*]

[a] *Department of Interface Chemistry and Surface Engineering,*
Max-Planck-Institut für Eisenforschung GmbH, 40237 Düsseldorf, Germany
[b] *Leiden Institute of Chemistry, Leiden University, Leiden 2300 RA, The Netherlands.*
[c] *Laboratoire de Physique des Solides, C.N.R.S., Université Paris-Sud, 91405 Orsay, France*
[d] *Institute for Materials, Ruhr-Universität Bochum, 44801 Bochum, Germany*
[e] *Helmholtz-Institute Erlangen-Nürnberg for Renewable Energy (IEK-11),*
Forschungszentrum Jülich GmbH, 91058 Erlangen, Germany
[f] *Department of Chemical and Biological Engineering, Friedrich-Alexander-Universität*
Erlangen-Nürnberg, 91058 Erlangen, Germany

[*] *Corresponding authors: geiger@mpie.de, cherevko@mpie.de*
[†] *These authors contributed equally to this work*

Supplementary Note 1 - Leaching processes and electrochemical procedures

Supplementary Table 1. Quantification of the leaching process of all studied perovskite powders during the first 60 s of contact with 0.1 M $HClO_4$. Total amount of the respective elements and dissolved weight percentage are given as well. Supplementary Fig. 1 shows the related experimental data.

Ba_2NdIrO_6

Element	Total / ng	Leached / ng	Leached /w%
Ba	114	66	58%
Nd	60	33	55%
Ir	80	24	30%

Ba_2PrIrO_6

Element	Total / ng	Leached / ng	Leached /w%
Ba	114	85	75%
Pr	58	44	76%
Ir	80	33	41%

Ba_2YIrO_6

Element	Total / ng	Leached / ng	Leached /w%
Ba	114	51	45%
Y	37	17	46%
Ir	80	28	35%

Sr_2YIrO_6

Element	Total / ng	Leached / ng	Leached /w%
Sr	72	37	51%
Y	37	18	49%
Ir	80	31	39%

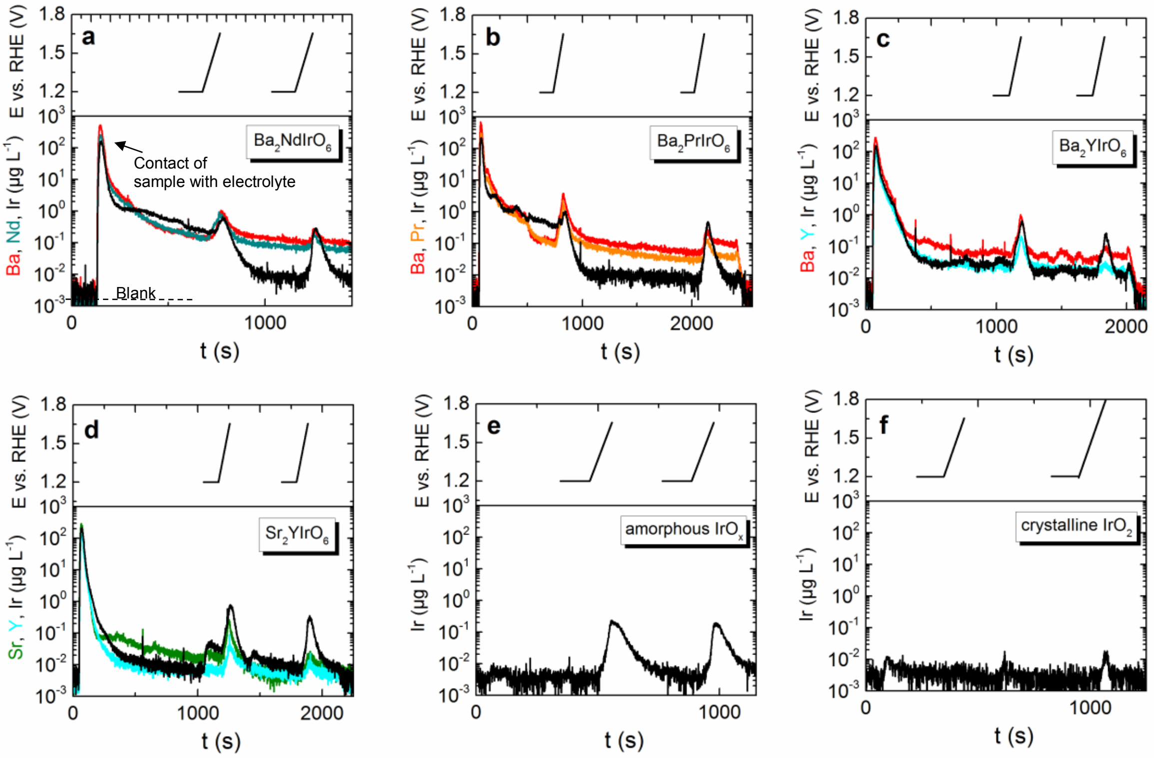

Supplementary Figure 1. Dissolution profiles of the investigated powder materials during initial contact at open circuit potential (potential not measured) and two contiguous potential sweeps (5 mV s^{-1}) to 1.65 V_{RHE}. High initial dissolution with fast decay is assigned to the formation of a passivating iridium oxide shell. Lower values for iridium dissolution compared to the other elements (see Supplementary Tab. 1) and X-ray photoemission spectroscopy performed in an earlier work[1] underline this statement as well. Measurements carried out in 0.1 M $HClO_4$.

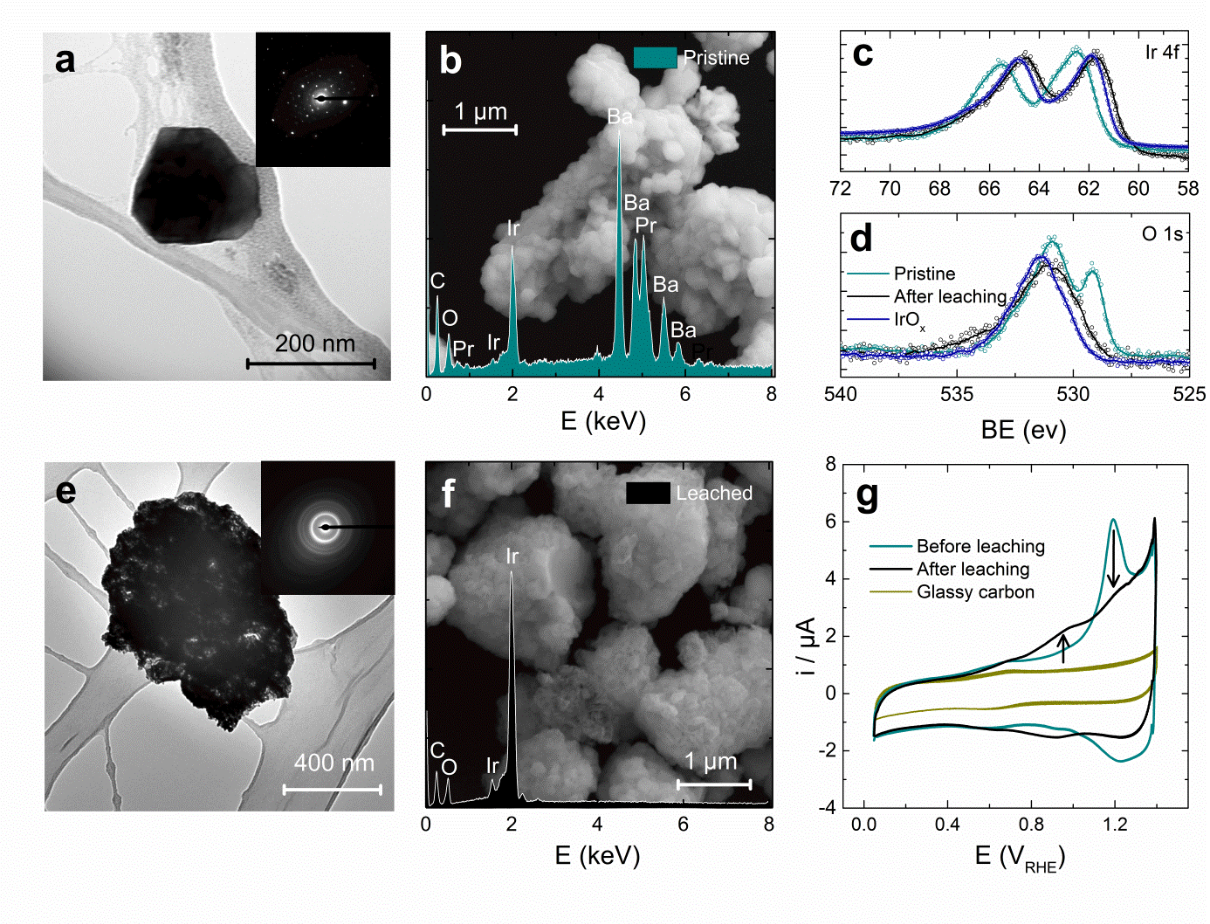

Supplementary Figure 2. Pristine Ba_2PrIrO_6 and Ba_2PrIrO_6 after leaching in 0.1 M $HClO_4$ for 14 days. Transmission electron microscopy (TEM) images of pristine (**a**) and leached (**e**) Ba_2PrIrO_6; inset shows the respective selected area electron diffraction (SAED) patterns. (**b+f)** Energy dispersive X-ray spectroscopy (EDS) with the respective scanning electron microscopy (SEM) images. (**c**+**d)** X-ray photoemission spectroscopy (XPS) showing the core-level spectra of the Ir 4f and the O 1s. (**g)** Cyclic voltammetry of the pristine and leached Ba_2PrIrO_6 (in this case 5 days leaching in 0.1 M $HClO_4$).

The penetration depths of SAED and TEM are expected to be higher than the diameter of the investigated particle, hence, leaching and formation of amorphous iridium oxide is not restricted to the surface. Prolonged leaching showed a significant decrease of the Ir^{IV}/Ir^{V} redox couple in the cyclic voltammogram, while Ir^{III}/Ir^{IV} increases (Supplementary Fig. 2g). Furthermore, the Ir 4f level is shifted towards lower binding energies after the leaching (Supplementary Fig. 2c). Both facts could be attributed to the formation of pure amorphous iridium oxide and a collapse of the initial structure.

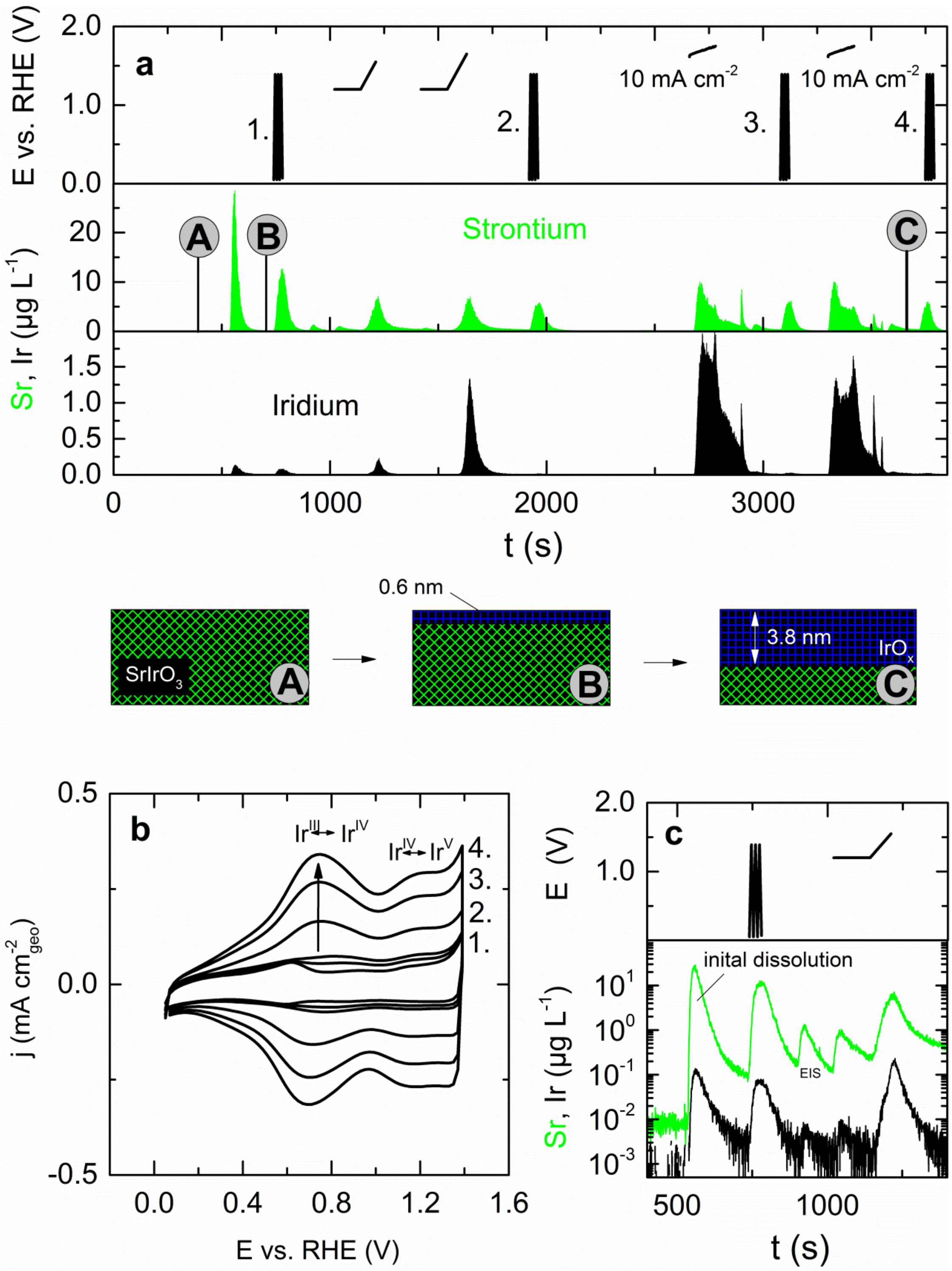

Supplementary Figure 3. In situ dissolution study on a SrIrO$_3$ film during electrochemical measurements. (**a**) Dissolution trends of Sr (*middle row*) and Ir (*bottom row*) with respect to the applied electrochemical program (*upper row*). Data plotted on the same time scale. The development of an Ir-rich and Sr-poor surface film can be calculated based on the density and the dissolved amounts of Ir and Sr. The results at three (A, B, C) representative positions are presented schematically. (**b**) Cyclic voltammograms (200 mV s^{-1}) recorded at different times in the electrochemical program. Numbering refers to CVs shown in (**a**). (**c**) Logarithmic plot of the dissolution shown in (**a**).

Supplementary Note 2 - Scanning electron microscopy of powders

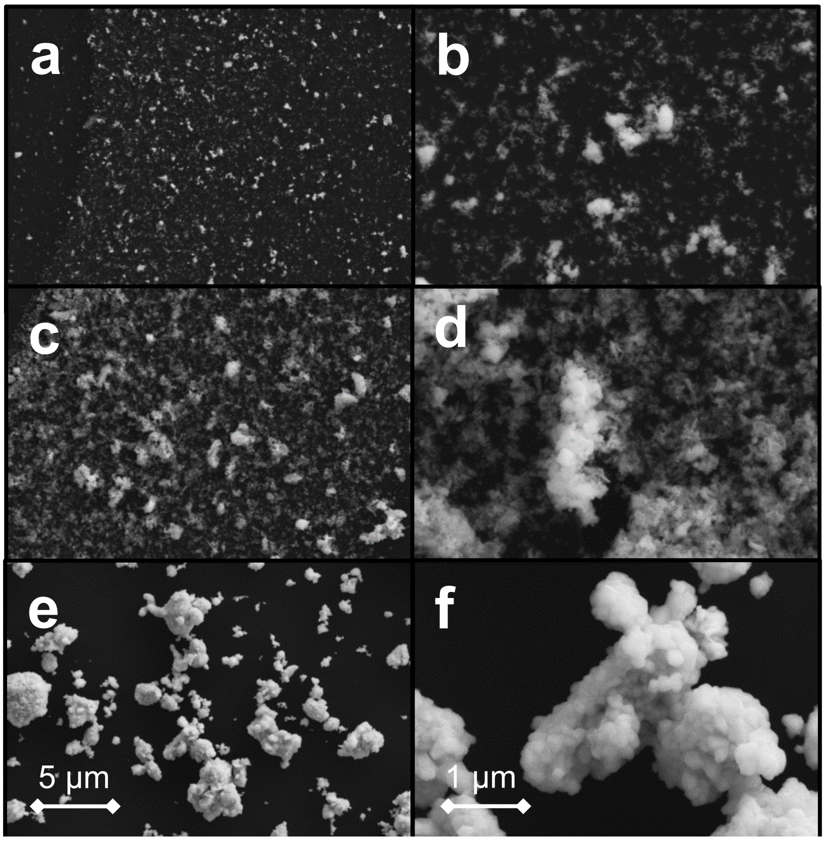

Supplementary Figure 4. SEM-images of crystalline IrO_2 (**a**,**b**), amorphous IrO_x (**c**,**d**) and Ba_2PrIrO_6 (**e**,**f**) presented in two different magnifications.

Even though perovskite particles tested in this work are large in size (see Supplementary Fig. 4), high OER-activities were obtained, which is another indication on the formation of a very active and highly porous structure.

Supplementary Note 3 - Normalization of OER-activity

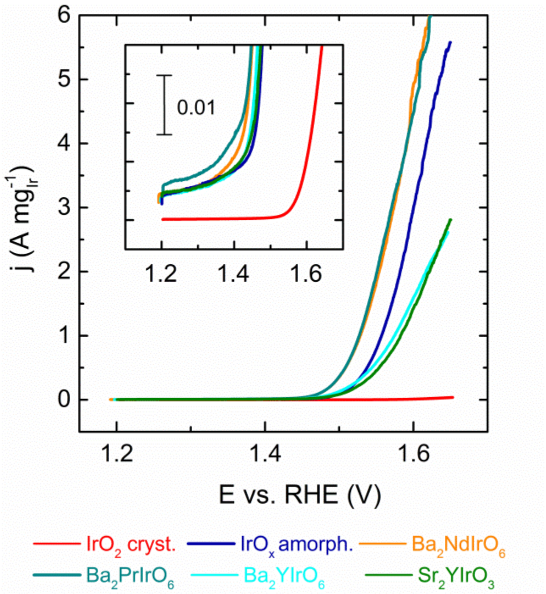

Supplementary Figure 5. OER-activity of the investigated powder materials recorded with a linear scan of potential at 5 mV s^{-1} in 0.1 M $HClO_4$ purged with Ar. Current is iR-corrected and normalized by actual mass of iridium, taking into account initial leaching of perovskites.

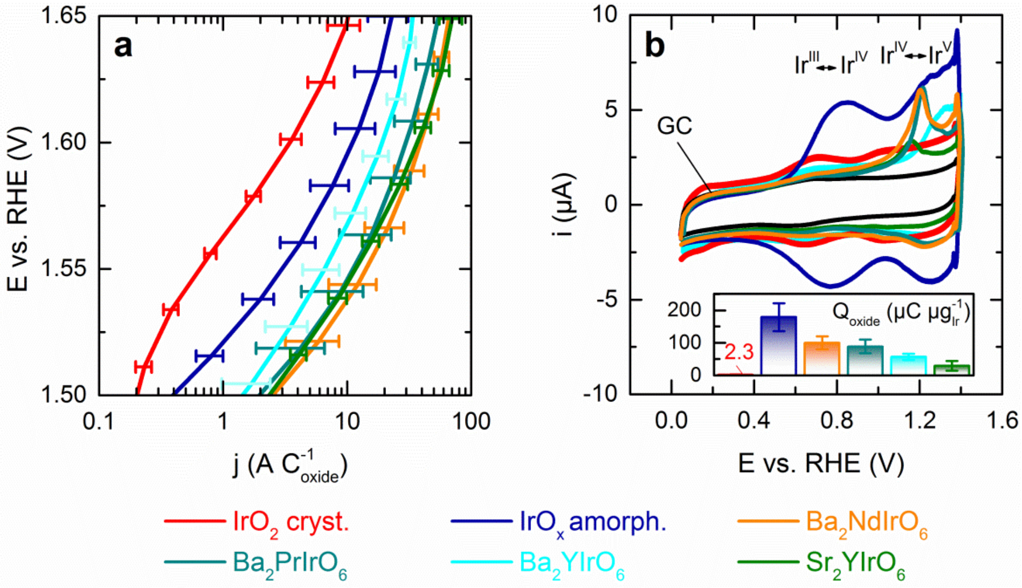

Supplementary Figure 6. Comparison of the investigated powder materials in terms of activity and specific surface area. (**a**) OER-activity recorded with a linear scan of potential at 5 mV s^{-1}. Current is normalized to the pseudocapacitive charge in the anodic scan between 0.4 and 1.3 V_{RHE} at 200 mV s^{-1}. (**b**) Cyclic voltammograms recorded with 200 mV s^{-1}, inset: charge in the anodic scan (0.4 - 1.3 V_{RHE}) normalized by actual mass of iridium taken into account the initial loss of iridium due to leaching in perovskites. All error bars were obtained using standard deviation of at least 3 independent measurements.

Enhanced pseudocapacitive charge (see inset Supplementary Fig. 6b) reveals that more active species are involved in the case of Pr- and Nd-based perovskites compared to Y-containing perovskites. Charge normalization, however, results in very similar activities for Ba_2PrIrO_6, Ba_2NdIrO_6 and Sr_2YIrO_6. Hence, the activity is not related to the chosen rare earth element, but rather to the amorphous structure that forms after leaching. Lower activities were achieved for Ba_2YIrO_6, which could be related to a slightly deviating CV shape.

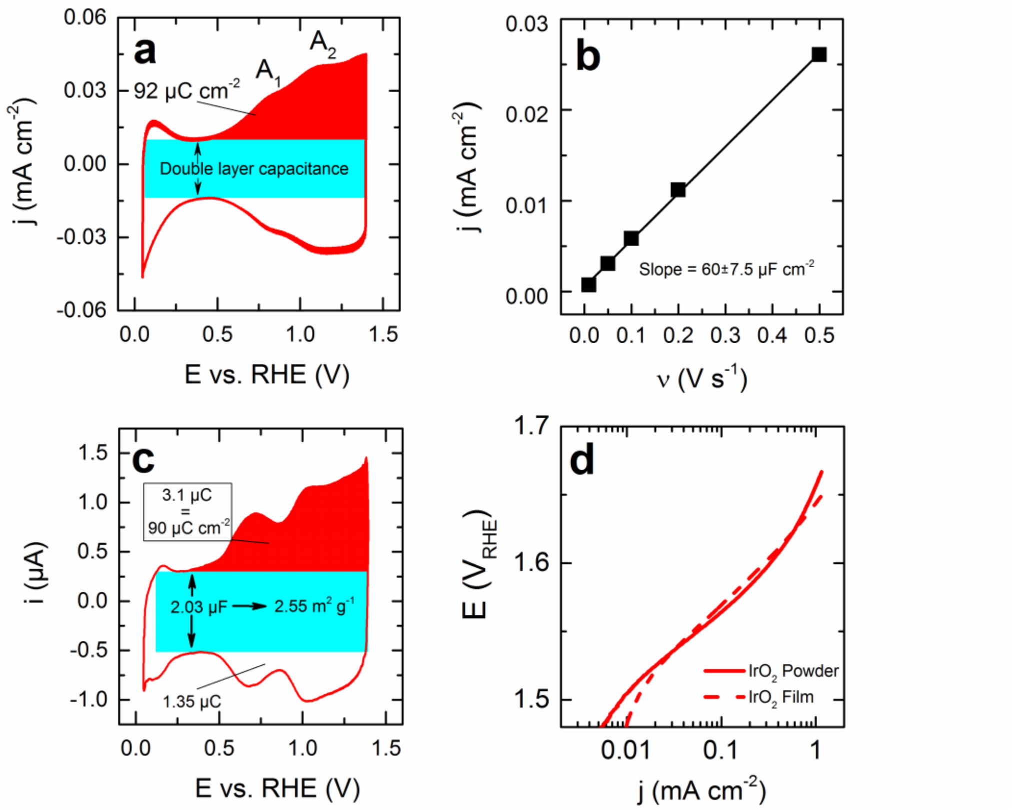

Supplementary Figure 7. Comparison of IrO_2 film and IrO_2 powder. (**a**) CV at 200 mV s^{-1} of IrO_2 film. (**b**) Current density in the double layer region plotted vs. scan rate. The resulting specific capacity of ~60 µF cm^{-2} is highlighted. (**c**) CV at 200 mV s^{-1} of IrO_2 powder. Background of the supporting glassy carbon electrode was subtracted. (**d**) OER activity of IrO_2 powder and IrO_2 film normalized to real surface area.

Assuming an ideally flat IrO_2 film, a specific double layer capacity of ~60 µF cm^{-2} was determined and used for the estimation of the IrO_2 powder surface area. We observed a specific surface area for IrO_2 powder of 2.5 m^2 g^{-1}. This value is in line with BET surface analysis for the same material by Pfeifer *et al.*[2] (2 m^2 g^{-1}). IrO_2 powder and IrO_2 film show the same activity normalized to real surface area (see Supplementary Fig. 7d). This could be an indication for no significant impact of defect sides or alike, which should be present in powders. The reason for good accordance of BET surface and electrochemical surface is the fact, that only the surface of IrO_2 is participating in the reaction. Furthermore, the material is a metallic conductor in the whole potential range enabling surface estimation via double layer capacitance.

In contrast to that amorphous iridium oxides are electrochromic and turned "off" at low potentials, making it impossible to estimate their surface area in this region by double layer capacitance. Furthermore, the active sites inside the porous 3D-layer are not reachable by BET surface analysis. Still, iridium oxides do have characteristic redox transitions which could be used for quantification. Assuming each active iridium centre in amorphous iridium oxide undergoes the transition from Ir^{III} to Ir^{V} normalization to charge should give a fair comparison as presented in the manuscript. However, 92 $\mu C\ cm^{-2}$ measured for crystalline oxide rather disproves, that all surface atoms undergo such transition. Theoretical values are in the range of 200 to 500 $\mu C\ cm^{-2}$ depending on the orientation of the surface. Another issue is the increasing double layer capacitance during turning "on" of the amorphous oxide. As double layer and redox transition are superimposed a separation is difficult with cyclic voltammetry. Electrical impedance spectroscopy could be an option to approach this issue. To sum up, normalization of OER currents is explicitly difficult for these systems. With the described method, huge misinterpretations due to surface effects can be avoided, however, precise calculations of turn over frequencies (TOF) is not possible.

Supplementary Fig. 8 shows a more detailed comparison of the representative materials with respect to normalization to active sites and the resulting trend for OER-activity. Using the back-scan in the CV, current arising from the onset of OER can be avoided and the whole potential range from 1.4 to 0.4 V vs. RHE can be used to quantify the active sites. Even though the anodic and cathodic branch do not mirror each other for double perovskites, the charge is approximately the same (see Supplementary Fig. 8b).

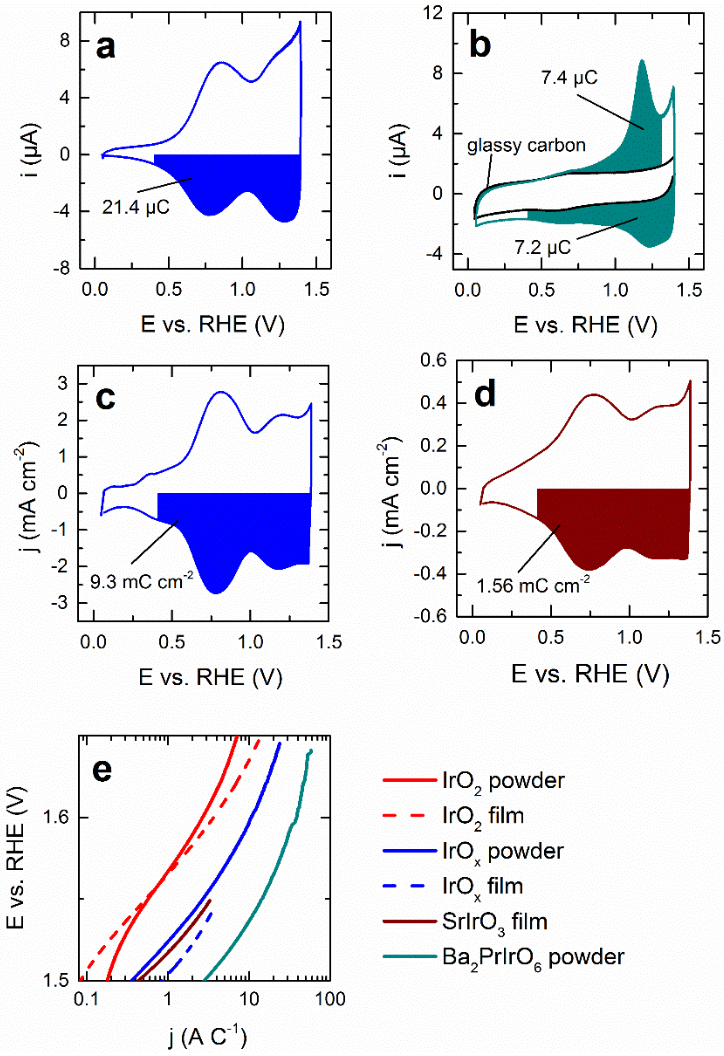

Supplementary Figure 8. Normalization by pseudocapacitive charge. (**a-d**) CVs at 200 mV s^{-1} in 0.1 M $HClO_4$. Area used for normalizing the OER current is highlighted. (**a**) IrO_x powder; (**b**) Ba_2PrIrO_6 powder; (**c** IrO_x film; (**d**) $SrIrO_3$ film (leached). (**e**) OER activity normalized to charge.

Supplementary Note 4 - The Stability-number

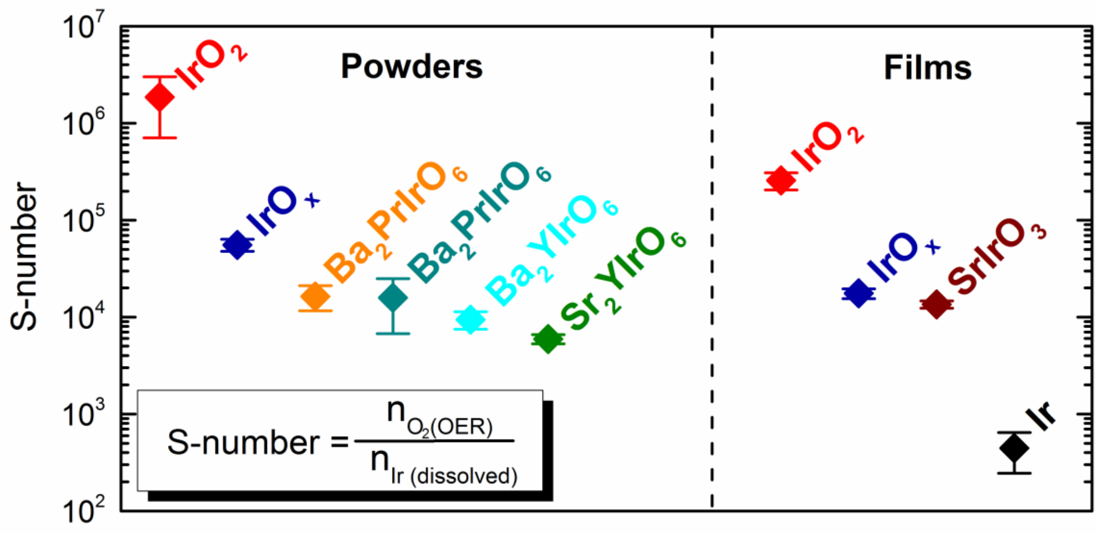

Supplementary Figure 9. Stability-number (ratio between amount of produced oxygen (calculated from total charge) and dissolved iridium) presented for all investigated powder and film materials based on a slow potential sweep (5 mV s^{-1}) to 1.55 V vs. RHE for films and 1.65 V vs. RHE for powders. To overcome the detection limit of the ICP-MS the upper potential limit was increased for crystalline IrO_2 to 1.65 V vs. RHE and 1.8 V vs. RHE for the IrO_2 film and IrO_2 powder, respectively. All measurements were carried out in 0.1 M $HClO_4$ purged with argon. Error bars were obtained by standard deviation of at least 3 independent measurements.

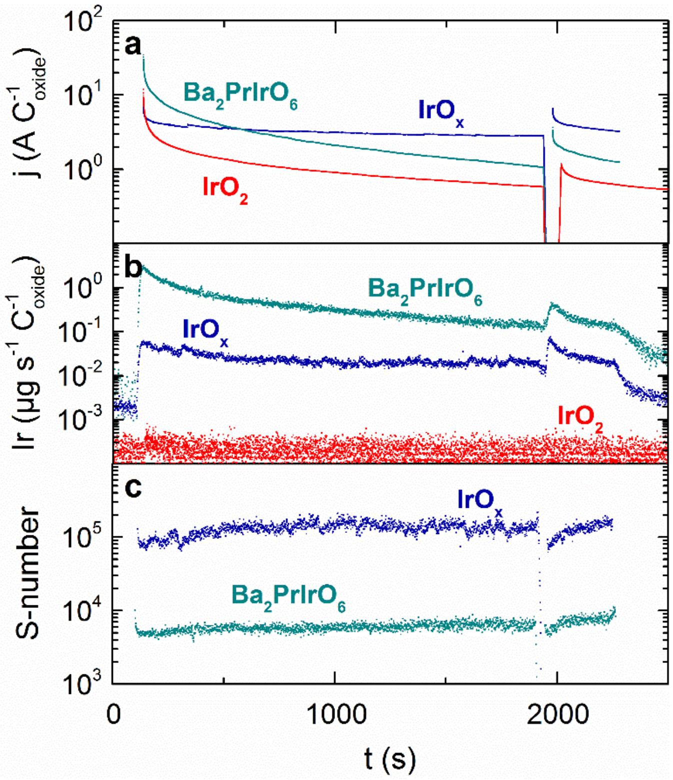

Supplementary Figure 10. Chrono-amperometry at 1.6 V vs. RHE. (**a**) Current profile, (**b**) dissolution profile and (**c**) calculated S-number. All data points are plotted against the same time axis. Dissolution of IrO_2 is below the detection limit. The decay in OER for Ba_2PrIrO_6 can be found as well in the respective dissolution profile, resulting in a constant trend for the S-number. The latter indicates on a direct relation of OER and dissolution.

As presented in Supplementary Fig. 9, a short linear scan with simultaneous tracking of dissolution can be beneficial for fast estimation of the Stability-number. However, initially dissolving defects and alike will influence the results. Still, for most materials the S-numbers investigated during longer polarization are in good agreement with the ones presented in Supplementary Fig. 9. For instance, IrO_x and Ba_2PrIrO_6 show very stable S-numbers over 30 min of polarization (see Supplementary Fig. 10), which are in the same range as presented in Supplementary Fig. 9. However, deviations were observed for IrO_2 films which stabilize during longer operation (S-number increases to 1.0 E+7; compare Fig. 7 in the manuscript). The latter expresses the need of longer polarizations and tracking of possible stabilization phenomena, as performed in Supplementary Fig. 11.

Supplementary Fig. 11 shows an exemplary measurement protocol for an IrO_x film, which was used in the same way for all the other materials in order to obtain the data presented in Fig. 7 in the manuscript. Initially the dissolution is higher and stabilizes after a few minutes. The stabilization process is slower for lower current densities. The tendency of slightly lower S-numbers at low current densities, presented in the manuscript is most likely an effect of not completely steady state dissolution. Note, to underline the meaningfulness of this approach, some current densities have been repeated in a non-stirred bulk cell over several hours with good accordance on the predicted dissolution rates by SFC-ICP-MS.

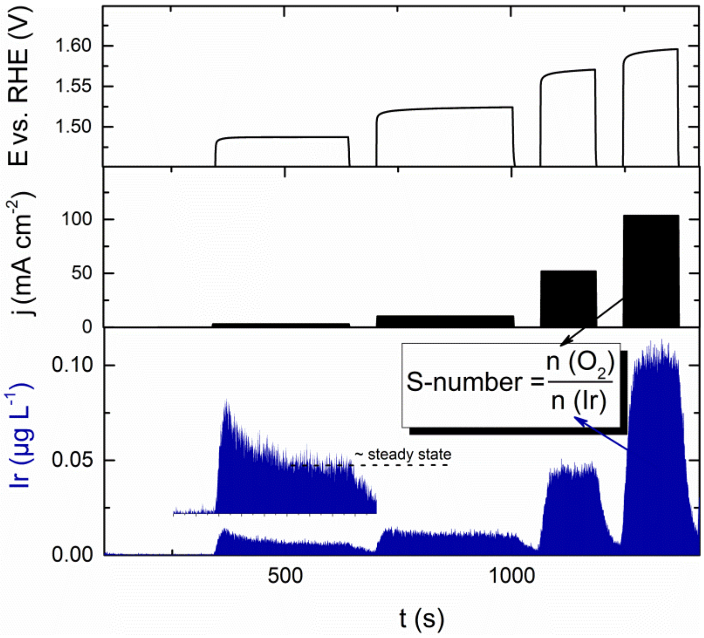

Supplementary Figure 11. Calculation of the S-number based on a SFC-ICP-MS measurement. Exemplary shown is the measurement on a hydrous iridium oxide film in 0.1 M $HClO_4$.

Supplementary Note 5 - Mechanistic insights

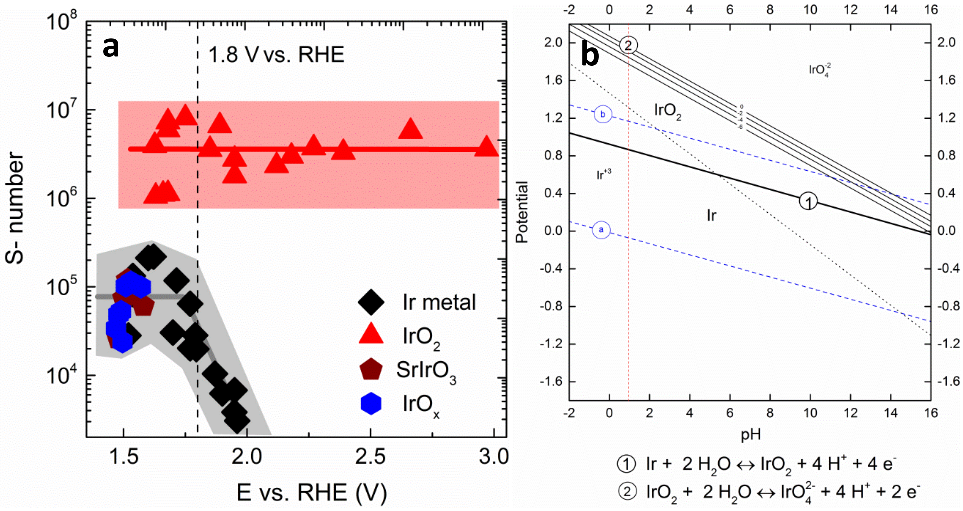

Supplementary Figure 12. (**a**) S-number plotted against potential. (**b**) Pourbaix diagram of iridium[3].

According to Supplementary Fig. 12a, the thermodynamically predicted dissolution reaction pathway forming IrO_4^{2-} is operative on iridium metal, which is oxidized electrochemically. Indication on this is the significant decrease of the S-numbers at potentials above 1.8 V vs. RHE. The origin of this can only be explained by a pure dissolution reaction:

$$IrO_2 + 2\,H_2O \rightarrow IrO_4^{2-} + 4H^+ + 2e^- \qquad (1)$$

In contrast to that rutile IrO_2 does not undergo this reaction pathway even at potentials around 3 V vs. RHE. It can therefore be concluded that it is significantly kinetically hindered as the thermodynamically favourable state would be IrO_4^{2-}. Still, IrO_3 and its hydration to IrO_4^{2-} can be the reason for its measurable dissolution. However, not as a separate potential dependent degradation reaction as described in equation (1), but independent of potential as soluble intermediate in the OER cycle[4].

The amorphous oxides (IrO_x and $SrIrO_3$) generally show low stability. Kinetic stabilization at higher potentials is therefore unlikely and we assume similar behaviour to iridium metal.

At low potentials it takes much longer to reach steady state dissolution on iridium metal as oxidation is still ongoing. Dissolution of iridium metal according to equation (2) would as well lower the S-number and explains these findings and the very low S-number of non-oxidized metallic iridium presented in Supplementary Fig. 9 for a short potential sweep.

$$Ir \rightarrow 3Ir^{3+} + 3e^- \qquad (2)$$

Note that a passivation of metallic iridium at potentials >1.8 V vs. RHE is not possible, resulting in a complete dissolution of 60 nm iridium films within 10 min!

Supplementary Note 6 - Comparison of the estimated lifetime with PEM-stacks

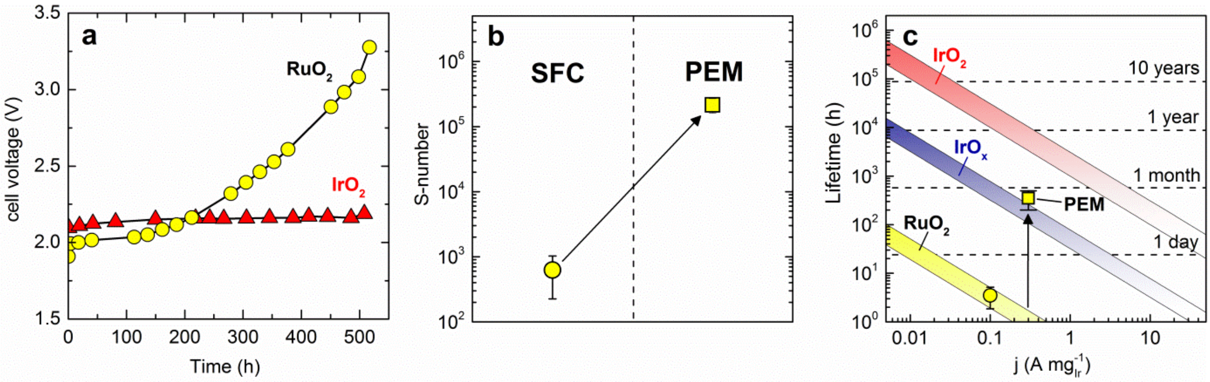

Supplementary Figure 13. Stability of RuO_2 obtained from SFC measurements in comparison to a PEM-stack. (**a**) Cell potential of a PEM-stack operated at 1.8 A cm^{-2} with a catalyst loading of 6 mg cm^{-2}; data replotted from Ayers *et al.*[5] (**b**) S-numbers for RuO_2 observed from SFC and extracted from the PEM stack, assuming the degradation is predominantly a cause of the catalyst dissolution. For the study in the PEM-stack RuO_2 was purchased from the same supplier without further treatment. (**c**) Calculation of the catalyst lifetime based on the S-number.

The question, whether the presented data of electrochemical half cells are relevant for real PEM electrolysers, is discussed on the basis of Supplementary Fig. 13, where a significant difference between stability of the same material in two environments is presented. Data on the end of life of real PEM-stacks is rare. Usually the presented results are limited to the period of constant performance. However, one example was reported by Ayers *et al.*[5] using RuO_2. The data is replotted in Supplementary Fig. 13a and compared with measurements of the same catalyst (commercial anhydrous RuO_2 (Alfa Aesar)) studied in the SFC. The lifetime of the PEM-stack differs more than two orders of magnitude in comparison to the one calculated from the dissolution obtained in the SFC (e.g. 1 h vs. 1 month). Hence, a lifetime estimation based on the S-number in the SFC is not directly relevant for application as it does underestimate the stability. This difference opens a new research topic in finding reasons for this difference. The results could be used for further improvement of the catalyst stability in an PEM-stack configuration.

Main factors that might cause the deviation between electrochemical half cell and PEM-stack are:

(i) Local acidity near catalyst's active centers in the MEA vs. acidity of the electrolyte used in electrochemical half cells (standard: pH = 1).

(ii) Diffusion of ions out of the coated membrane vs. diffusion of ions out of a thin catalyst film without membrane. Higher concentration of dissolved species close to the catalyst surface in a membrane assembly would lower the dissolution rate based on thermodynamics, assuming that reaction is diffusion controlled.

(iii) Possible (re)-deposition processes of the transferred away from the dissolution place dissolved ions. It is important to distinguish between deposition in the membrane or the cathode, which would be equal to a loss of active material causing additional degradation of the membrane, and re-deposition on other active catalyst particles or supports on the anode, which would not lead to a performance loss.

A further evaluation of the reasons behind this difference is planned to be the content of a future work.

Supplementary Methods - The Scanning Flow Cell

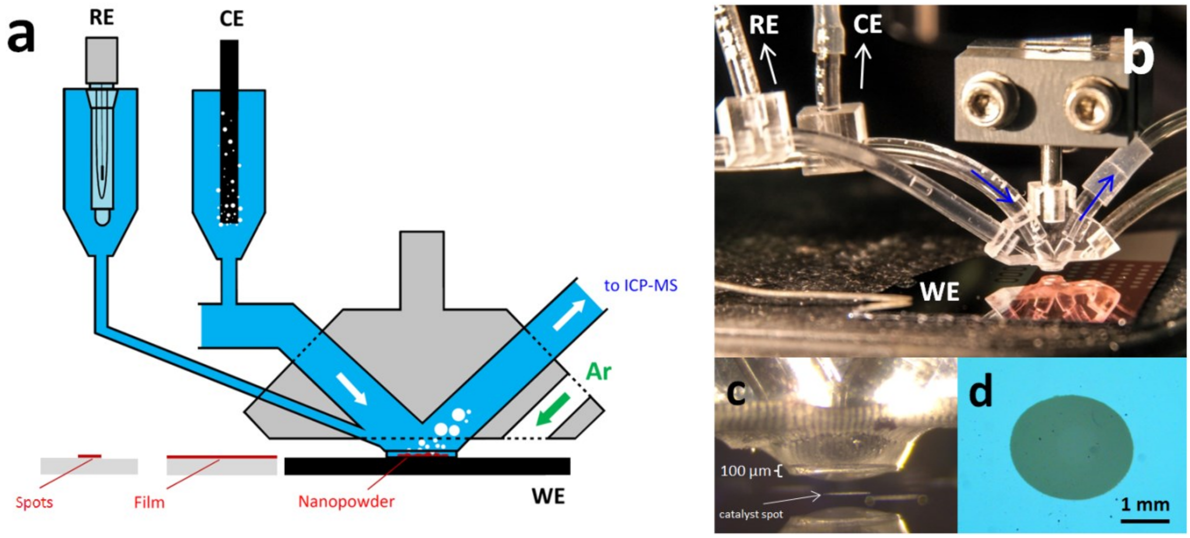

Supplementary Figure 14. (**a**) 2-D scheme of the scanning flow cell (SFC) with three different sample types used in this work. (**b**) Image of the SFC with an opening diameter of 2 mm approaching a sample with 1 mm diameter iridium spots. (**c**) Magnification of the SFC-plateau and the silicon sealing while approaching a powder catalyst spot. The thickness of the silicon sealing is highlighted. Underneath a hanging meniscus of electrolyte is visible. (**d**) Print of the SFC opening with an area of 0.035 cm^2. The image shows an oxidized iridium surface formed by continuous potential cycling.

Supplementary References

1 Diaz-Morales, O. *et al.* Iridium-based double perovskites for efficient water oxidation in acid media. *Nature communications* **7**, 12363 (2016).

2 Pfeifer, V. *et al.* The electronic structure of iridium and its oxides. *Surface and Interface Analysis* **48**, 261-273 (2016).

3 Pourbaix, M. *Atlas of electrochemical equilibria in aqueous solutions*. (National Association of Corrosion Engineers, 1974).

4 Kasian, O., Grote, J. P., Geiger, S., Cherevko, S. & Mayrhofer, K. J. J. The Common Intermediates of Oxygen Evolution and Dissolution Reactions during Water Electrolysis on Iridium. *Angewandte Chemie* **57**, 2488-2491 (2018).

5 Ayers, K. E., Dalton, L. T. & E.B., A. Efficient Generation of High Energy Density Fuel from Water. *ECS Trans.* **41**, 27-38 (2012).